Nanoscale

PAPER

View Article Online
View Journal | View Issue

Cite this: *Nanoscale*, 2020, **12**, 21376

Size dependent influence of contact line pinning on wetting of nano-textured/patterned silica surfaces

H. Gokberk Ozcelik,[a] Ezgi Satiroglu [b] and Murat Barisik *[a]

Wetting behavior on a heterogeneous surface undergoes contact angle hysteresis as the droplet stabilized at a metastable state with a contact angle significantly different from its equilibrium value due to contact line pinning. However, there is a lack of consensus on how to calculate the influence of pinning forces. In general, the pinning effect can be characterized as (i) microscopic behavior when a droplet is pinned and the contact angle increases/decreases as the droplet volume increases/decreases and (ii) macroscopic behavior as the pinning effects decrease and ultimately, disappear with the increase of the droplet size. The current work studied both behaviors using molecular dynamics (MD) simulation with more than 300 different size water droplets on silica surfaces with three different patterns across two different wetting conditions. Results showed that the contact angle increases linearly with increasing droplet volume through the microscopic behavior, while the droplet is pinned on top of a certain number of patterns. When we normalized the droplet size with the corresponding pattern size, we observed a "wetting similarity" that linear microscopic contact angle variations over different size heterogeneities continuously line up. This shows that the pinning force remains constant and the resulting pinning effects are scalable by the size ratio between the droplet and pattern, independent of the size-scale. The slope of these microscopic linear variations decreases with an increase in the droplet size as observed through the macroscopic behavior. We further found a universal behavior in the variation of the corresponding pinning forces, independent of the wetting condition. In macroscopic behavior, pinning effects become negligible and the contact angle reaches the equilibrium value of the corresponding surface when the diameter of the free-standing droplet is approximately equal to 24 times the size of the surface structure. We found that the pinning effect is scalable with the droplet volume, not the size of the droplet base.

Received 19th July 2020,
Accepted 22nd September 2020

DOI: 10.1039/d0nr05392a

rsc.li/nanoscale

1. Introduction

Surface wetting is pivotal in numerous applications involving interfacial phenomena. Manipulating wetting behavior is fundamental for self-cleaning surfaces, micro/nanofluidic devices, and heat exchangers to control mass, momentum, and heat transport through the interfaces. Surface patterning is commonly employed to tune the surface characteristic due to the proven impact of surface structures on wetting and related physics.[1] Various techniques such as electrochemical deposition,[2] laser texturing,[3] crystallization control,[4] and photolithography have been employed to create surface patterns in various forms from the micro to nanoscale. Results show that even relocating a single atom can affect surface wetting. However, the understanding and characterization of wetting on a heterogeneous surface are not yet complete.

Classically, wetting on a rough surface is classified into two different conditions as the Wenzel state and Cassie–Baxter state. The homogeneous wetting of a liquid filling the Groves of the surface roughness is described as the Wenzel state.[5] The Wenzel model calculates an apparent contact angle from the intrinsic angle of an ideal surface given by Young's equation as a function of increased surface area due to roughness. On the other hand, an incomplete wetting is the Cassie–Baxter state[6] where the liquid remains on top of the surface roughness. The contact angle is predicted by considering the fractional surface area wetted. There exist also hybrid states; in the case of surface heterogeneity in different length scales, a dual-scale wetting develops. For instance, hierarchical surface roughness in the form of nanoscale structures over the microscale roughness of a rose petal undergoes Cassie–Baxter at the nanoscale and Wenzel at the microscale which yields a hydrophobic surface but with a high adhesion. However, recent

[a]*Department of Mechanical Engineering, Izmir Institute of Technology, Izmir, 35430, Turkey. E-mail: muratbarisik@iyte.edu.tr*
[b]*Department of Energy Systems Engineering, Izmir Institute of Technology, Izmir, 35430, Turkey*

experimental and theoretical studies showed that rough surface wetting behavior is more complex and there are many situations that cannot be explained by the Wenzel and Cassie–Baxter models. Such a shortcoming is fundamentally due to the missing information about the applicability limits of these theories in terms of comparable size of the liquid droplet to roughness size, while these models assume that surface roughness is much smaller than the droplet size.

One of the most important unsolved issues of heterogeneous wetting is contact angle hysteresis. In most of the literature studies, wetting hysteresis is viewed from the perspective of kinetics. Owing to its first discovery from dynamic experiments, advancing and receding contact angles are defined from the shape of a moving droplet. In this motion of contact line, the liquid–solid cohesion determines the advancing angle while the liquid–solid adhesion identifies the angle for receding. On the other hand, a similar contact angle hysteresis also develops in the case of a static droplet stabilized at a metastable state on a heterogeneous surface with a contact angle significantly different from its equilibrium value. Here, surface heterogeneity creates contact line pinning yielding metastable contact angles in a maximal and minimal range ascribed to advancing and receding contact angles for a droplet with a constant contact area. For example, a pinned contact line keeps the base of the droplet constant during increasing droplet volume, which eventually yields an increase in the contact angle (Fig. 1). The so-called pinning force creates an energy barrier for the contact line to overcome in order to move from one metastable state to another.[7] When the droplet volume continues to increase, depinning of the contact line develops which might increase or decrease the wetting angle. Later, pinning of the contact line to the adjacent pattern occurs which might again increase or decrease the contact angle.[8] In the literature, there is an agreement that increasing liquid–solid interaction strength, higher disjoining pressure and sharper surface geometry[9] increase the pinning. However, there is a lack of consensus on how to calculate or define the contact angle under the influence of pinning forces. This is mostly due to two major unsolved questions: (i) does the effect of pinning depend on the relative size of the droplet to surface heterogeneity length scale? and (ii) does the effect of pinning increase or decrease the contact angle compared to its equilibrium value free from the hysteresis? In other words, the size limit for pinning effects to become negligible and the general contribution of pinning force are still unknown.

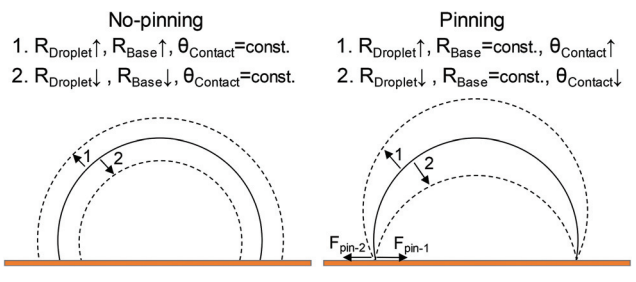

Fig. 1 Illustration of the droplet shape change during the increase and decrease of the droplet volume with and without contact line pinning.

Regarding the first question, researchers found pinning hysteresis as a 1-D issue originated from interactions at the liquid/solid/gas triple contact line[10,11] independent of the contact area[12] between the liquid and solid. They demonstrated this behavior by theoretical derivations in comparison with the experiments[13] for a case where the pinning spot (*i.e.* a single surface heterogeneity) is under the droplet but away from the contact line. In such a case, pinning effects do not develop and the resulting contact angle is equal to predictions of Young's equation since the rest of the surface is flat. Also validating that the pinning is a contact line issue, studied cases are very specific and different from an average heterogeneous surface. More natural equally distributed surface heterogeneity was also studied by many to describe the dominant effect of pinning. Increasing the width of inhomogeneity is found to create higher pinning which shows that the inhomogeneity size determines the pinning effects.[14] Similarly, the pinning was found to be decreased with decreasing the surface roughness[15] or size of the chemical heterogeneity.[16] It was concluded that pinning effects become dominant when the size of the droplet becomes comparable[15] to the size of the roughness. A recent study carried this discussion further by devising a theoretical description for pinning and concluded that the droplet size should be equal to or larger than 40 times[17] of the characteristic roughness scale for conventional theories to become applicable. This is an important conclusion for the literature; however, the occurrence of this theoretical observation has never been studied/validated by any experiment or molecular dynamics simulations.

Regarding the second question, researchers have attempted to extend existing theories to include the pinning force exerted on the contact line to predict its influence. However, suggested models are still far from providing a general description. This is mostly due to the fact that two distinct behaviors develop during the contact angle hysteresis. First, for increasing droplet volume, the contact angle changes with a constant base radius in the pinned regime and after a certain droplet size, a drastic change of the contact angle develops due to depinning followed by pinning at the next spot and repeating this cycle back again; these can be called "microscopic behavior". Secondly, due to the strength and influence of this microscopic variation, the pinning decreases and ultimately disappears with an increase in the droplet size, which can be described as "macroscopic behavior". Even though both of these behaviors are governed by the droplet diameter, characterization of microscopic states with pinning–depinning transitions and their variation in macroscopic behavior is very hard to obtain. The major challenge here is missing explicit interpretation of the pinning force. A possible experimental measurement of pinning force requires distinguishing it from the solid/liquid and solid/vapor surface tensions, which is very challenging. Instead, the current literature estimates the corresponding pinning force backwards from the change of the measured contact angles during a droplet volume change

which might be due to an increase of the droplet volume or decrease by evaporation. We should underline here that a thorough calculation requires pre-knowledge of the equilibrium contact angle of the corresponding surface free from the hysteresis. For such a case, researchers observed an increase of pinning force with increasing volume, for instance, in a given microscopic state up to a maximum pinning force which was found as a property of the corresponding solid/liquid couple.[18,19] In the macroscopic perspective, pinning force is found to decrease with increasing droplet volume with a "sawtooth-like oscillation" through the pinning and depinning behaviors.[17] From parallel to pinning force calculations, researchers also try to generalize its influence. For example, the first question is whether the equilibrium contact angle free from the hysteresis is in the range of maximum and minimum contact angles of the pinning hysteresis. We should define this equilibrium angle better here to determine if it is in the Wenzel or Cassie–Baxter state and calculated from the corresponding models. Some studies[20,21] mentioned that the contact angle becomes independent of its equilibrium value through pinning, but some others presented that the equilibrium value is in between the contact angle range that pinning might be both increasing and/or decreasing the contact angle through the microscopic state. For example, in the case of the Wenzel state, the contact angle was found to increase due to pinning effects.[22] We illustrated a general behavior of pinning effects in Fig. 2 based on these observations from the literature. We simply added a possible equilibrium contact angle in between two pinning states for comparison purposes. These results show that pinning force might be a positive and/or a negative value creating lower and/or higher contact angles compared to the equilibrium contact angle estimated from conventional wetting theories. Although there are multiple conclusions that appear appropriate for different conditions, a complete understanding of the influence of the pinning is still missing.

This paper aims to present the development of both microscopic and macroscopic wetting behavior of pinning hysteresis between water and silica using molecular dynamics simulations. Three different surface structures will be studied under two different hydrophobic and hydrophilic wetting conditions determined by changing the liquid/solid interactions. The size of the water droplet will be varied between 1 nm and 15 nm in diameter while droplets containing up to 15 000 water molecules will be modeled for every surface and wetting case. The current objective requires an extended wetting modelling of more than 300 simulation cases. Ultimately, we will provide characterization of the pinning effect as a function of the ratio of the roughness size to droplet size and an estimation for the equilibrium contact angle free from the hysteresis.

2. Nanoscale wetting

In addition to our main objective to characterize pinning effects at varying droplet and surface heterogeneity sizes, we want to also provide an important understanding on variation of equilibrium wetting behavior by changing surface structures at the nanoscale. Nanoscale wetting is important to resolve hierarchical wetting mechanisms, or nucleate boiling and condensation of nanodroplets. Further size dependent complications need to be considered in the characterization of nanoscale wetting as observed by both experiments[23,24] and molecular level simulations.[25–27] Besides the contact angle hysteresis, two major mechanisms affect the wetting behavior at the nanoscale and yield deviations from the classical description of Young's equation. As the droplet size decreases, (i) the "line tension" along the three-phase contact line becomes increasingly important[28] while (ii) the liquid–vapor interface surface tension changes as a function of curvature and "Tolman length".[29] The current literature modified Young's equation to include line tension[30] and Tolman correction[31] as a function of radius of three-phase line (r_B) and radius of droplet (R) as,

$$\gamma_{SV_\infty} = \gamma_{SL_\infty} + \gamma_{LV_\infty}\left(1 - 2\frac{\delta}{R}\right)\cos\theta + \frac{\tau}{r_B} \quad (1)$$

where γ_{SV_∞}, γ_{SL_∞} and γ_{LV_∞} are the interfacial tensions at the boundaries between the liquid (L), solid (S) and vapor (V) at macroscopic scales (∞), δ is the Tolman length, τ is the line

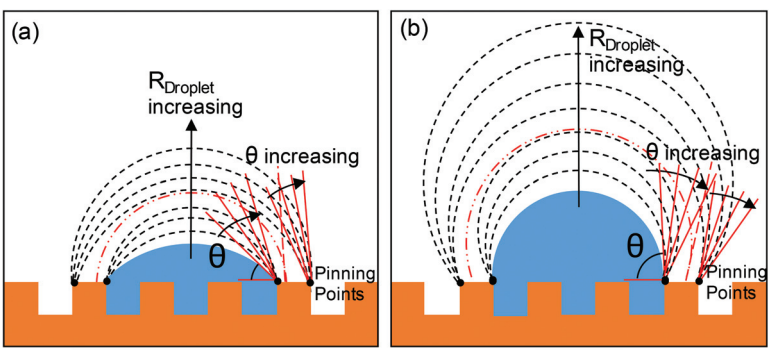

Fig. 2 Illustration of the contact angle change by growing droplets on a heterogeneous surface during pinning and depinning for two different surface wetting conditions of (a) hydrophilic and (b) hydrophobic.

tension between the droplet and surface, and θ is the microscopic contact angle. The microscopic contact angle, θ, can be defined in terms of the macroscopic contact angle as,

$$\cos\theta_\infty = \left(1 - 2\frac{\delta}{R}\right)\cos\theta + \frac{\tau}{r_B\gamma_{LV_\infty}} \quad (2)$$

which can be simplified into,

$$\frac{(R-2\delta)\gamma_{LV_\infty}\sin 2\theta + 2\tau}{\sin\theta} = 2R\gamma_{LV_\infty}\cos\theta_\infty \quad (3)$$

Eqn (3) estimates the contact angle of a nanoscale spherical droplet as a function of droplet radius. However, the corresponding Tolman length and line tension values are controversial. Multiple MD studies were dedicated to investigating size dependent behavior in nano-scale wetting.[32,33] In order to overcome these difficulties, it is a common practice for MD studies to simulate large enough cylindrical water droplets to obtain negligible curvature at the liquid–vapor interface and zero curvature at the three-phase line[34,35] to eliminate the Tolman and line tension effects from their measurements. Reported Tolman length values vary around ~0.05 nm for the water–vapor interface[36,37] that water droplets bigger than 1 nm in diameter develop negligible curvature influence on water surface tension.

For the inclusion of pinning effects, researchers further extended eqn (2) to consider the pinning force on the three-phase contact line. For a negligible Tolman length, the following form of equation is employed by multiple studies as a general description.[18,21]

$$\cos\theta = \cos\theta_\infty - \frac{\tau}{r_B\gamma_{LV_\infty}} - \frac{f_{pin}}{2\pi r_B\gamma_{LV_\infty}} \quad (4)$$

Eqn (4) estimates the microscopic contact angle from its macroscopic value as a function of line tension, base radius and pinning force (f_{pin}) per unit length of the contact line which is $2\pi r_B$ for a spherical droplet with base radius r_B. As described earlier, a direct calculation of pinning force is missing in the literature and existing estimations are based on eqn (4) and measured contact angles. For example, Wang and Wu[18] estimated pinning force as,

$$F_{pin} = \gamma_{LV_\infty}(\cos\theta - \cos\theta_\infty) \quad (5)$$

Here, the macroscopic contact angle, θ_∞, can be defined as $\gamma_{LV_\infty}\cos\theta_\infty = \sigma_f(\gamma_{SV_\infty} - \gamma_{SL_\infty}) - (1-\sigma_f)\gamma_{LV_\infty}$ based on the surface fraction of heterogeneity (σ_f) using the Cassie–Baxter model. They present that pinning force varies between each depinning event and a maximum pinning force can be defined from the receding contact angle as $F_{pin,\,max} = \gamma_{LV_\infty}(\cos\theta_{receding} - \cos\theta_\infty)$, after which the droplet moves to the next pinning spot. Studies also focused on this work of adhesion (w_a) through contact angle hysteresis as $w_a = \gamma_{LV_\infty}(\cos\theta_{receding} - \cos\theta_{advancing})$[38] which was later extended to study the minimum energy required for depinning at the molecular level, but it was found too complicated to be characterized.[39]

3. Molecular dynamics methodology

The most recent nano-technological applications ranging from targeted drug delivery[40] to nano-membranes[41] employ silica materials. As the nanoscale interactions between solid domains and liquids define the operation of these applications, we particularly focused on silica surfaces. While the experiments are challenging and expensive for nanoscales, molecular dynamics (MD) calculations have been a robust and reliable tool to provide insight into the nano-scale world. We utilized the LAMMPS (Large-scale Atomic/Molecular Massively Parallel Simulator) code[42] as the MD solver. The simulation domain is formed by a silica slab and a nano-scale water droplet. Similar to earlier MD studies,[43,44] we modeled the β-cristobalite form of silica since its molecular density is similar to the density of amorphous form of silica. The multibody Tersoff potential[45,46] is used to model silica intramolecular interactions. We used a SPC/E water model to simulate water molecules. Accordingly, the length of the OH bond and H–O–H angle were constrained with the SHAKE algorithm[47] as 0.1 nm and 109.47°, respectively. Oxygen and hydrogen atoms of water are charged with $0.4238e$ and $-0.8476e$, respectively. A 1 nm cut off distance was defined for both dispersive and coulombic interactions between water molecules. The particle–particle particle–mesh (PPPM) solver is used to evaluate long-range coulombic forces among water molecules combined with the Lennard-Jones (L-J) potential to model dispersive interactions as,

$$\Phi(r_{ij}) = 4\varepsilon_{ij}\left(\left(\frac{\sigma_{ij}}{r_{ij}}\right)^{12} - \left(\frac{\sigma_{ij}}{r_{ij}}\right)^{6}\right) + \frac{1}{4\pi\varepsilon_0}\sum_i^a\sum_j^b\frac{q_iq_j}{r_{ij}} \quad (6)$$

where r_{ij} is the intermolecular distance, ε is the depth of the potential well, σ_{ij} is the molecular size for interaction between two atoms, ε_0 is the dielectric constant for vacuum, and q_i values are the partial charges. Interaction parameters between similar materials were taken from the corresponding model. For example, interaction parameters between silica atoms were defined by the Tersoff model while interactions between water molecules were from the SPC/E model. On the other hand, for the interaction parameters between dissimilar molecules, it is a common practice through MD studies to estimate these parameters using various forms of mixing rules. For instance, the Lorentz–Berthelot (LB) mixing rule utilizes arithmetic mean for the molecular diameter and geometric mean for the potential strength. For example, for silicone–oxygen interactions, parameters can be calculated by the LB mixing rule given as,

$$\sigma_{Si-O} = \frac{\sigma_{Si-Si} + \sigma_{O-O}}{2},\ \varepsilon_{Si-O} = \sqrt{\varepsilon_{Si-Si}\times\varepsilon_{O-O}} \quad (7)$$

Using the corresponding parameters given in Table 1, the LB mixing rule predicts the interaction parameters σ_{Si-O} = 2.6305 Å and ε_{Si-O} = 0.12088 eV. However, the interaction parameters between identical molecules are optimized for a bulk

Table 1 Molecular interaction parameters used for the SPC/E water model

Molecule pair	σ (Å)	ε (eV)	q (e)
O–O	3.166	0.006739	−0.8476
H–H	0	0	0.4238
Si–O[49]	2.633	0.01511	0

material system, which may need to be re-parameterized for the interaction of nonidentical pairs instead of using mixing rules. For instance, our earlier wetting study based on MD measured contact angles of water nano-droplets showed that interaction parameters from the LB mixing rule do not create the wetting behavior of the corresponding surface. Multiple authors indicated their concerns and proposed ways to calculate the interaction parameters of non-identical molecules accurately.[48–53]

One methodology from the literature is to tune interaction parameters between water and the surface in order to recover the experimentally measured wetting angle. Such a methodology yielded very accurate interface modeling for graphene[54] and silicon[49] surfaces. A similar idea was employed for silica by Cruz-Chu *et al.*;[55] however, instead of changing the interface interactions parameters, the authors changed the potential depth of silicon–silicon interactions to tune the wetting, while continuing to use the mixing rule to calculate water and silica interaction parameters. Such a perspective still suffers from problems arising from the mixing rule and the interaction parameters are not transferable to any other MD simulations of silica/water systems.

As another methodology, interaction parameters between water and silica can be predicted from first principles calculations which is an up-to-date research. The most commonly used quantum mechanical approach is the Kohn–Sham density functional theory (DFT).[50] There are many criticisms about the accuracy of DFT. The standard DFT calculations fail to describe long-range electron interactions of the dispersion or the van der Waals (vdW) forces[56] such that additional corrections are needed in order to capture vdW forces in DFT calculations. An interesting analogy coined by Klimes and Michaelides classified and ranked the existing methods through the "stairway to heaven" from "the most approximate to the more sophisticated" approaches for long range dispersion interactions.[56] DFT-D1 and DFT-D2 were found to be inaccurate by many because they employ a constant dispersion coefficient and employ the earlier mentioned LB mixing rule for the estimation of the dispersion coefficient. The DFT-D3 group was designed to consider the environmental dependence of dispersion[57,58] and the Becke–Johnson (BJ) model[57,59,60] is found to yield fair estimations compared to the other models in this group. Just recently, we performed DFT calculations for the binding energy between a silica slab and a water molecule using the BJ model.[61] For the given crystal structure of silica, we calculated LJ estimated potential energy curves using eqn (8) and tuned its parameters by comparing the energies calculated by *ab initio* from the sites with pure, non-bonded interactions.

$$\Delta E = \sum_{i}^{\infty} 4\varepsilon_{\mathrm{Si-O_w}}\left(\left(\frac{\sigma_{\mathrm{Si-O_w}}}{r_{\mathrm{Si}_i-\mathrm{O_w}}}\right)^{12} - \left(\frac{\sigma_{\mathrm{Si-O_w}}}{r_{\mathrm{Si}_i-\mathrm{O_w}}}\right)^{6}\right) + \sum_{i}^{\infty} 4\varepsilon_{\mathrm{O_{Si}-O_w}}\left(\left(\frac{\sigma_{\mathrm{O_{Si}-O_w}}}{r_{\mathrm{O_{Si}}_i-\mathrm{O_w}}}\right)^{12} - \left(\frac{\sigma_{\mathrm{O_{Si}-O_w}}}{r_{\mathrm{O_{Si}}_i-\mathrm{O_w}}}\right)^{6}\right) \quad (8)$$

where subscripts Si, O_{Si} and O_w denote silicon atoms in silica, oxygen atoms in silica and oxygen atoms of the water molecule, respectively. The first term on the right-hand side calculates interactions between the oxygen of water and every Si atom of silica, while the second term on the right side calculates interactions between the oxygen of water and every oxygen atom of silica. Here, calculations of interactions between water and silica require four parameters. The interaction diameters can be estimated as the mean of vdW diameters of corresponding atoms while the interaction strengths between (i) silicon and oxygen of water, and (ii) oxygen of silica and oxygen of water will be the remaining unknowns. For such a case, we used the silicon–oxygen interaction strength value which was calculated to recover the experimentally measured hydrophobic behavior of silicon surfaces by our earlier MD study ($\varepsilon_{\mathrm{Si-Ow}}$ = 0.01511 eV), and then we estimated the interaction strength between oxygen of silica and oxygen of water from the DFT results. Calculated parameters were later tested in MD simulations of the water droplet on the silica surface. Although the resultant contact angle of silica surfaces was in the range of experimental studies, DFT was found to overestimate the interaction potentials similar to the conclusion of others from the literature.[51] For such a case, starting from the DFT results, we further parametrized the interaction of dissimilar oxygen atoms by an additional MD study in the current work. Experimental wetting studies of silica suggest a wide range of contact angles such as from 40° to 92° due to various surface conditions of silica.[55,62–64] We should also mention here that the wetting behavior of the current smooth β-cristobalite surface is assumed to be analogous to wetting behavior of amorphous silica surfaces while the recent studies measured 55° on amorphous silica with no surface processing.[65] Hence, we simulated a water droplet on the smooth silica surface and tuned $\varepsilon_{\mathrm{O_{Si}-O_w}}$ to determine two values recovering possible hydrophobic and hydrophilic behavior of silica at the contact angles of 55° ($\varepsilon_{\mathrm{O_{Si}-O_w}}$ = 0.0121 eV) and 95° ($\varepsilon_{\mathrm{O_{Si}-O_w}}$ = 0.00674 eV).

As discussed in chapter 2 in detail, nanoscale wetting develops size dependent behavior in liquid surface tension and due to line tension. We want to remove these two effects in order to measure pinning effects solely. For the first one, we kept droplet sizes a lot bigger than the Tolman length values for water (~0.05 nm).[36,37] To eliminate curvature related line tension effects, we created hemi-cylindrical water droplets with linear three-phase lines.

Hemi-cylindrical water droplets successfully formed on the selected single crystalline surfaces as given in Fig. 3. These

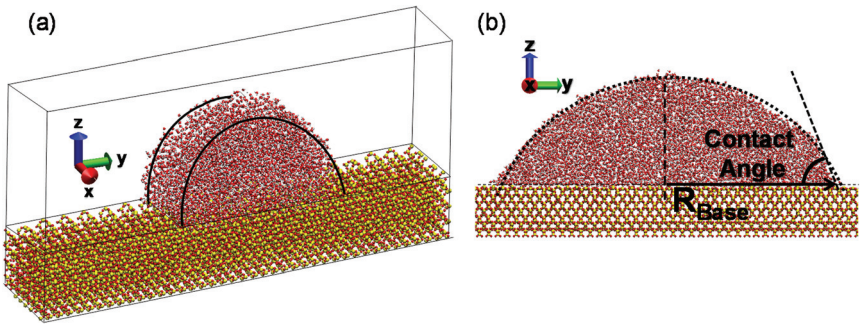

Fig. 3 (a) The snapshot of the simulation domain of flat silica with a hemi cylindrical water droplet. (b) Schematic of the contact angle on a snapshot. Oxygen, hydrogen, and silicon molecules are illustrated as red, white, and yellow spheres, respectively.

droplets extend through the periodic boundary. A periodic boundary condition was imposed on x and y directions while the z-direction was bounded with a specular reflection boundary. The Verlet algorithm was applied to integrate Newton's equation of motion with a time step of 0.001 ps. The bottom layer of the silica substrate was excluded from time integration to prevent any shift. At the beginning of wetting simulations, Maxwell–Boltzmann velocity distribution was assigned for all molecules at 300 K. The NVT ensemble with a Nosé–Hoover thermostat was applied to keep the temperature at 300 K. Simulations were carried out with 2×10^6 timesteps (2 ns) to reach an isothermal steady state. After that, a microcanonical ensemble (NVE) was employed to obtain averaging of the desired properties for 6×10^6 timesteps (6 ns). Averaging is performed with 5 ps intervals. Due to the hemi-cylindrical droplet shape, long rectangular prisms with a size of $\infty \times 0.1$ nm $\times$ 0.1 nm along x, y, and z directions were used to resolve droplets.

Water density was averaged by bins in a rectangular prism shape in the y–z plane. We optimized the system and bin size in order to obtain a sufficient density resolution with manageable statistical fluctuations. Two dimensional (2D) density contours which represent equally dense regions were extracted from bin-wise water. The molecular surface creates density layering[66] that the structure of the 2D density contours was found to be circular except in this near wall region. Contact angles were measured from these averaged density contours. First, the droplet boundary was determined as the points at which the density is half of bulk water (0.5 g cm^{-3}). This is based on the assumption that a possible "Gibbs dividing surface"[67] for the vapor–liquid interfaces lies approximately at the average of vapor and water densities similar to earlier definitions.[68–70] Second, we fit a circle passing through the points 0.8 nm above the surface. Near wall density points closer to the surface than 0.8 nm were omitted to avoid the influence from density fluctuations at the liquid–solid interface. Finally, the radius of the circle was denoted as r_{droplet} while r_{base} was defined at which the circle meets the solid substrate. Using these, contact angles were geometrically calculated.

4. Results and discussion

In addition to having similar solid density with amorphous silica, the structure of the β-cristobalite silica form has further advantages due to its unique crystal structure. The β-cristobalite is in a periodic self-repeating honeycomb structure which can be nano-patterned in 2 dimensions by simply disconnecting crystalline structures in a row to obtain a naturally repeating pattern sequence. For such a case, we systematically created three different surface structures by removing an equal number of silica molecules through a row in y- and z-directions and described these surfaces by the number of crystalline structures disconnected. Simply, if a single crystalline structure is removed in both directions, the surface is named R_1; but if two crystalline structures are removed, that surface is named R_2. All different surfaces are given in Fig. 4.

Hemi-cylindrical droplets of various sizes were developed on each surface for two different water silica interactions of hydrophilic and hydrophobic conditions. We observed the variation of the contact angle with the change of the droplet size while the droplet base radius remained constant. As an example, snapshots of molecular systems of droplets of four different sizes on the R_1 surface with high and low wetting conditions are given in Fig. 5. All these different size droplets have approximately the same base radius, as they sit on a similar number of surface structures. From here, we will name one hill and one valley of surface structure as a unit surface pattern. Hence, droplets in Fig. 5 are all on five surface patterns. For the hydrophilic surface, the contact angle increases from 53.5° to 66.4° degree (Fig. 5(a)–(d)) with the increase of the droplet volume described by the number of water molecules modeled, for simplicity. For the hydrophobic case, the contact angle rises from 96.0° to 106.3° with the increase of the water size (Fig. 5(e)–(h)). Clearly, contact line pinning develops which restrains the droplet at its position yielding an increase in the contact angle. An interesting result here is that, on a hydrophilic surface, the addition of 250 water molecules causes 13° change in the contact angle, but in the low wetting case, only a 10° rise develops with the addition of approximately 650 water molecules. We should also underline that

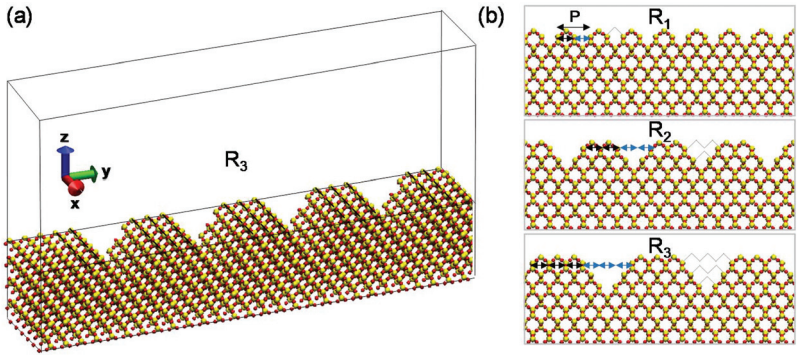

Fig. 4 Nano-patterned silica surface (a) in 3-dimensional view. (b) Different size surface patterns.

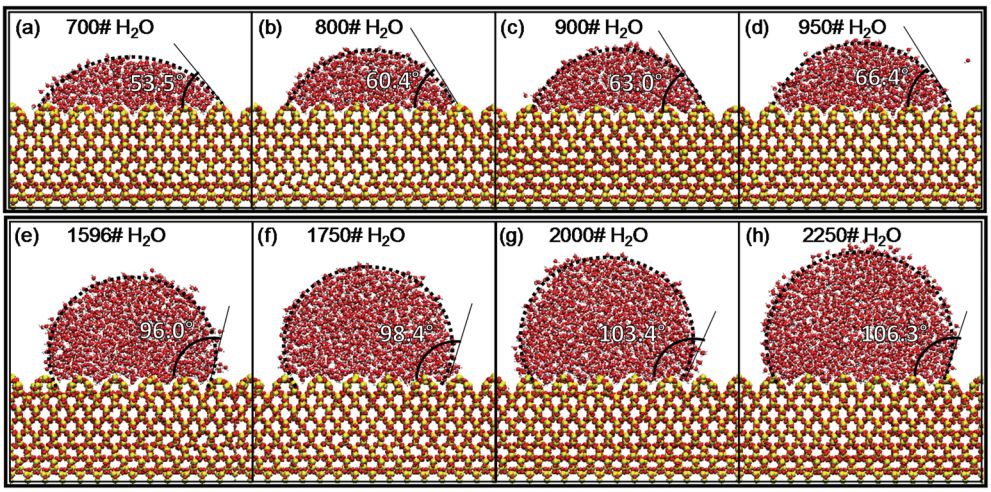

Fig. 5 Variation of the wetting angle on the R_1 surface for different size droplets with a constant base radius covering 5 surface pattern sets. Top row (a), (b), (c) and (d) are under hydrophilic conditions and bottom row (e), (f), (g) and (h) are under hydrophobic conditions.

contact angles measured under these high and low wetting conditions on the flat silica surface case with no pattern were 55° and 95° and showed no size dependence. Hence, we also observed the effect of surface patterning here; but the question is what is the equilibrium contact angle of the corresponding surface pattern independent of pinning effects? We observed from the literature that many studies on the wetting of patterned surfaces are eventually not at their equilibrium and under the effect of pinning.[71,72]

We conducted a great number of simulation cases to resolve the pinning effects on both microscopic and macroscopic behavior. At a certain microscopic state as the droplet sits on a certain number of surface patterns, we applied very precise increments in the droplet size to capture the complete variation in the contact angle and eventually the depinning behavior preciously. For the macroscopic extent, we increase the droplet size as much as our computational resources allowed to reach the highest droplet size possible. We performed all these for three different surface heterogeneities under two different wetting conditions. For example, we presented density contours of three different droplet sizes for three different base sizes with contact angle measurements in Fig. 6 for R_1 surface heterogeneity. Nine measurements on the left are for the hydrophilic condition (Fig. 6(a_1), (b_1), (c_1), (d_1), (e_1), (f_1), (g_1), (h_1) and (i_1)) and nine results on the right are for the hydrophobic condition (Fig. 6(a_2), (b_2), (c_2), (d_2), (e_2), (f_2), (g_2), (h_2) and (i_2)). The R_1 surface develops contact angles similar to the contact angle of the smooth surface (55°), but the wetting angle increases with the increase of the droplet size up to a certain value, after which the droplet base expands and the contact angle decreases back. This behavior continues in the next microscopic state. We observed that the maximum contact angle through a given microscopic state gradually increases with the increase in the base diameter. A different behavior was observed in the hydrophobic surface cases. While the lowest contact angles are similar to the smooth hydrophobic surface value (95°) and the contact angle increases with an increase in the droplet size, the maximum contact angle of each microscopic state decreases different from the low wetting behavior.

Contours of water droplets on the R_2 surface are presented in Fig. 7. In this case, droplets sitting on 3, 4, and 5 patterns

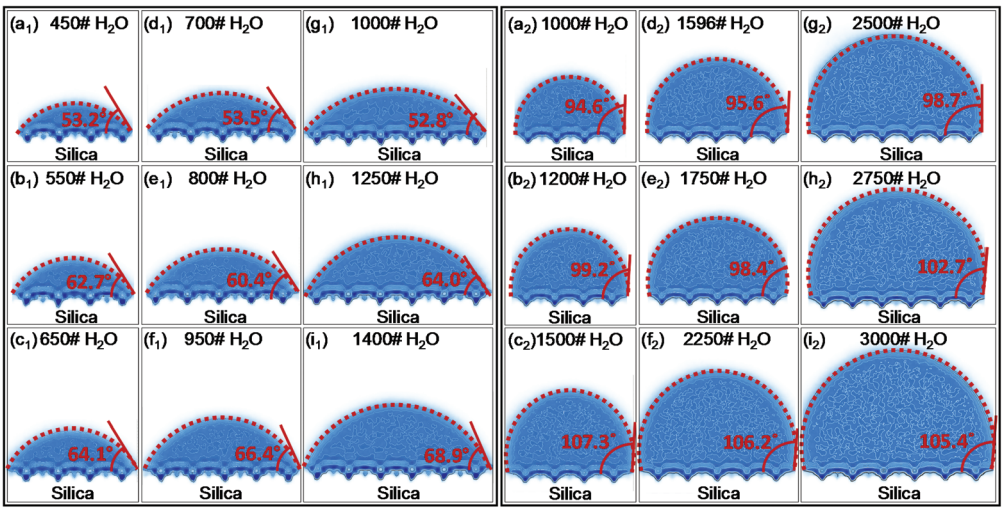

Fig. 6 Density contours of different droplet sizes and corresponding contact angles on the R_1 surface. Subscripts 1 and 2 refer to hydrophilic and hydrophobic conditions, respectively.

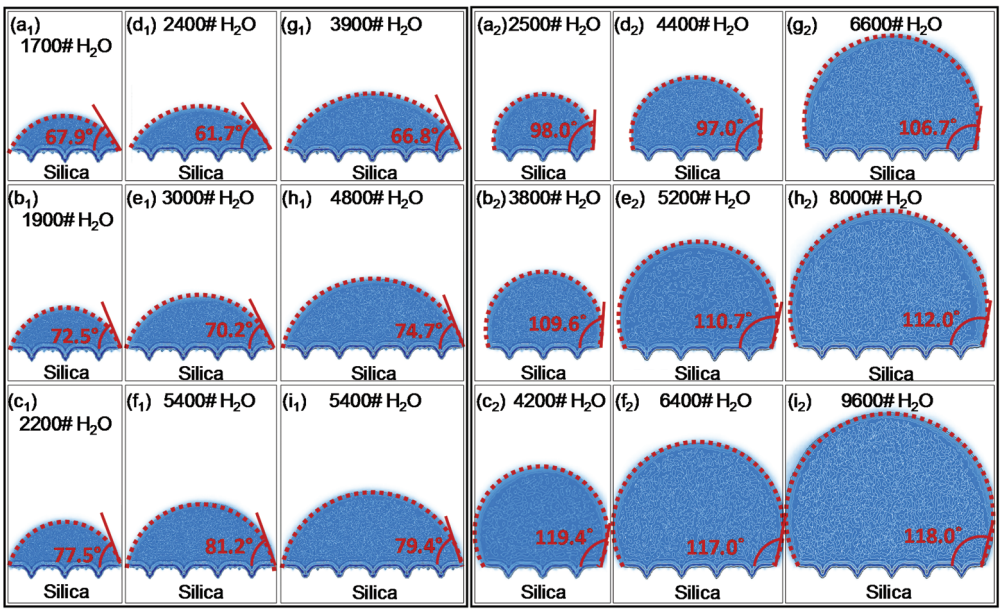

Fig. 7 Density contours of different droplet sizes and corresponding contact angles on the R_2 surface. Subscripts 1 and 2 refer to hydrophilic and hydrophobic conditions, respectively.

are given. Even though we reached a droplet diameter of 11 nm, the surface pattern size doubles compared to R_1 that the maximum pattern number covered was able to reach 9 for the hydrophilic condition and 6 for the hydrophobic condition for this roughness case. Overall, measured contact angles on R_2 are higher than the results of the R_1 surface. Through each microscopic state, minimum contact angles are higher than the corresponding flat surface results and the maximum contact angles reached are a lot higher than the results of the R_1 surface for both hydrophilic and hydrophobic conditions. This is a simple sign that surface wetting decreased with the increase of surface heterogeneity. For the understanding of the macroscopic behavior, we hypothesized and practiced another way of characterization. We compared the contact angles of the droplets sitting on the same number of patterns on R_1 and R_2 surfaces. Simply, we checked for a possible "similitude" between different size droplets over different size heterogeneities when the ratio of droplet size to heterogeneity size is the same. The current surface patterning actually is very advantageous since we can change the size of the periodically repeating structure while keeping its shape the same. At this point, we could not observe any similarity; this is mostly due to the difference in the possible equilibrium contact angles of these different surface structures. The pinning effects are observed

in a wide range of sizes that it will be important to present a general behavior of heterogeneity influence independent of the scales.

We further presented density contours and wetting angles of the R_3 surface case (Fig. 8). We reached our computational limit with 15 000 water molecules for a 14 nm diameter water droplet over three surface patterns under the hydrophobic condition. Hence, we could be able to simulate only two microscopic states of the hydrophobic case with droplets sitting two and three surface patterns only. Overall, contact angles showed a substantial increase at this roughness level that the hydrophobic case yielding droplet size independent 95° on a smooth surface develops a wetting angle as high as 135° under the effect of both surface heterogeneity and pinning. Furthermore, the hydrophilic case (55° over the flat surface) became hydrophobic with the wetting angle as high as 98°.

We present all of the contact angles measurements over R_1, R_2, and R_3 in Fig. 9 as a function of droplet volume. Here, we calculated a radius for the given cylindrical droplet from its volume and described it as the free-standing radius ($R_{D\text{-}FS}$) which is independent of the droplet's wetting shape. A similar idea was practiced by an earlier study[12] where they theoretically described that the volume of the droplet is the determining factor for the contact angle variation under pinning,

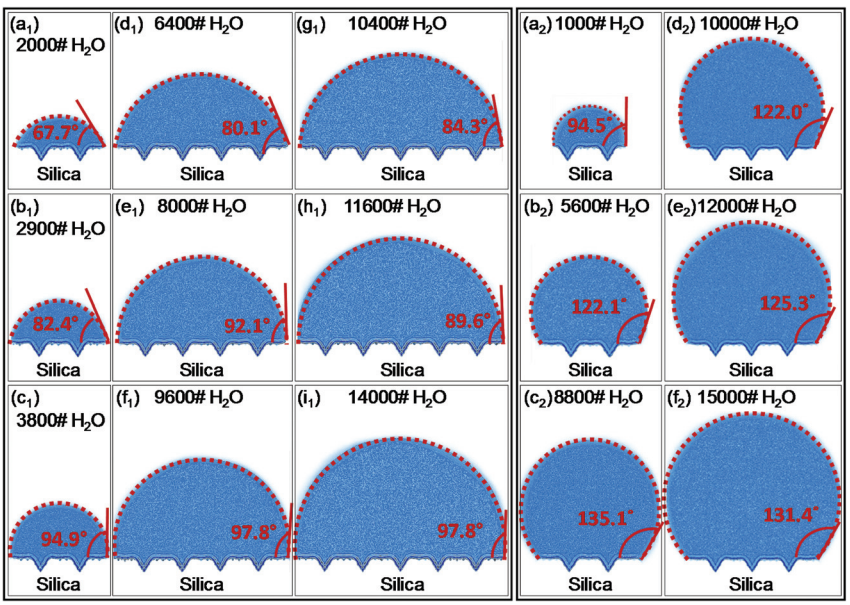

Fig. 8 Density contours of different droplet sizes and corresponding contact angles on the R_3 surface. Subscripts 1 and 2 refer to hydrophilic and hydrophobic conditions, respectively.

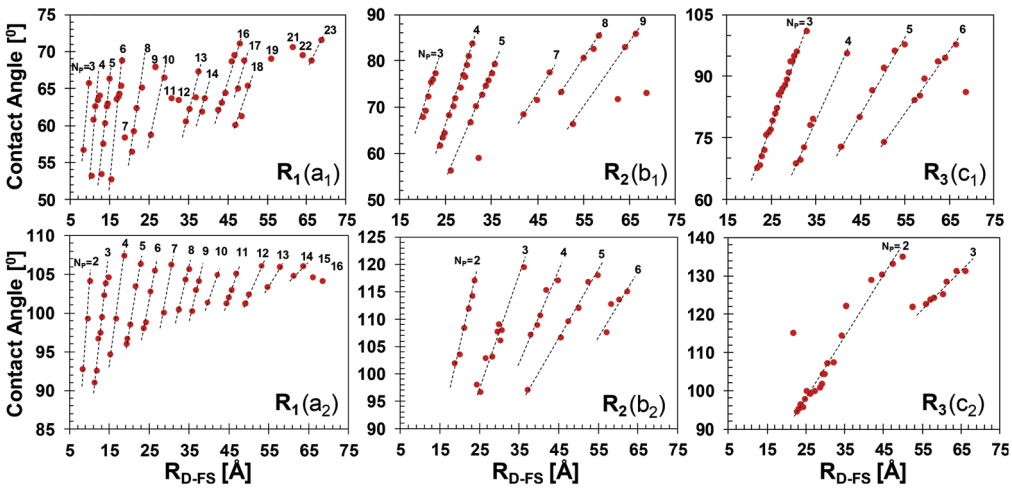

Fig. 9 Variation of the contact angle as a function of droplet volume on various surface heterogeneities and under different wetting conditions described by subscripts 1 and 2 for hydrophilic and hydrophobic conditions. Dashed lines connect contact angle measurements on the same number of patterns while the insets on top give the number of occupied patterns.

instead of the diameter of the circle that the droplet formed on the surface during wetting. The first row is under hydrophilic conditions (Fig. 9(a_1), (b_1), and (c_1)), while the second is under hydrophobic conditions (Fig. 9(a_2), (b_2), and (c_2)). There are more than 300 contact angle measurements here at various droplet sizes and surface roughness and under various wetting conditions. When the droplet is pinned and stays on the same number of patterns during growing droplet size through the microscopic behavior of pinning effects, we observed that the contact angle changes linearly. This is consistent for more than 60 microscopic states which are specified by dashed lines. We also labeled each microscopic state with its number of surface patterns in Fig. 9. For instance, for the R_1 hydrophilic surface in Fig. 9(a), we were able to create 12 complete microscopic states. Starting from three surface patterns, growing water droplet covers up to 23 surface patterns. There are also multiple single cases which could not form a complete set; for the remaining figures we did not label their number of patterns. Droplets of the same size cover less patterns due to the decrease in their base area under hydrophobic conditions. As a second important observation, we saw that the slope of these linear microscopic contact angle variations consistently decreases with the increase of the droplet size, in other words, with the increase of surface patterns under the droplet. These two main conclusions are consistent for all 3 different surface heterogeneities under two different wetting conditions: hydrophilic and hydrophobic.

When we look into details of contact angle variation under pinning forces, we observe that the influence of pinning is different depending on both surface heterogeneity and wetting conditions. For instance, the overall range of maximum and minimum contact angles measured increases with the increase of surface heterogeneity under both hydrophobic and hydrophilic conditions; but we observed that the measured contact angle range widens more with increasing roughness through the hydrophobic wetting cases. We can conclude here that pinning effects at a microscopic level become dominant with increasing surface heterogeneity and decreasing surface wetting.

Secondly, the variation of the wetting angle with the increase of the droplet size at a given microscopic state is dominant for small droplets, and this variation decreases with the increase of numbers of patterns covered by the droplet. Simply, the difference between the maximum and minimum contact angles of a certain microscopic state decreases when the droplet size becomes large compared to the size of the pattern. Here, these maximum and minimum angles become closer to each other and eventually, converge to a certain value which appears to be specific for the given surface. This value that contact angles approaching by growing droplet size is the equilibrium wetting angle of the corresponding surface pattern and wetting condition through the macroscopic behavior of pinning effects. The maximum droplet size that we can model is restrained by the computation limitations, but we could be able to observe most of the macroscopic behavior over the R_1 surface under the hydrophilic condition by reaching up to 23 surface patterns covered. Through its macroscopic behavior, the maximum and minimum angles of R_1 increase from one microscopic state to other with increasing droplet size while the difference between maximum and minimum angles drops as low as few degrees. We can conclude that the R_1 hydrophilic surface converges to its equilibrium value with an increasing projectile angle through fluctuating contact angles; the equilibrium contact angle is higher than all of the maximum contact angles reached at microscopic states. On the other hand, we could only attain an utmost 18 surface pattern coverage with the similar droplet sizes for the hydrophobic R_1 surface; but the corresponding macroscopic behavior can be almost observed. When the R_1 surface becomes hydrophobic, a very different influence of pinning develops on the macroscopic behavior of the same set of droplets; the minimum contact angle of microscopic states decreases while the maximum angles also slightly lessen. Here, through the fluctuating contact angles, the hydrophobic surface converges to its equilibrium value, which eventually lies in between maximum and minimum contact angles of its microscopic states. In the other surface heterogeneities, the same size droplets can cover less with the increase of pattern size that we can only observe a limited part of the macroscopic behavior. Regardless of this, the conclusions above appear to be consistent through these cases as well.

In an attempt to characterize the pinning effects, we normalized the droplet sizes with the pattern size of the corresponding surface. Here, we used the droplet size as the free-standing cylindrical droplet radius ($R_{D\text{-}FS}$) which is a function of droplet volume only. We presented cosine of the contact angles of different sized droplets on different surface heterogeneities as a function of the normalized droplet size ($R_{D\text{-}FS}/P$) in Fig. 10.

The contact angles measured on R_1, R_2 and R_3 surfaces under hydrophilic conditions are plotted together in Fig. 10(a) as a function of $R_{D\text{-}FS}/P$. With the increase of contact angle, cos (θ) decreases and even reaches negative values when the contact angle becomes higher than 90°. The microscopic states with a wider range of angle variation appear in a low $R_{D\text{-}FS}/P$ range. Simply, results of large droplets on top of large heterogeneities grouped together with the results of small droplets over narrow heterogeneities. For simplicity, we only have contact angles of the complete microscopic sets and did not include the single cases. In Fig. 10, we observed that the linear variations through different microscopic states of different size heterogeneities continuously line up if they are at the same number of pattern coverage. This is very interesting and one of the most important outputs of the current study. As an example, we present the density contours of droplets on 5 surface patterns and corresponding unified linear contact angle variation (Fig. 11(a)) while the droplet and surface structure sizes are changing but the ratio between the droplet base area and pattern size is remaining constant (R_{base}/P = constant). The continuous microscopic behavior observed at a constant number of pattern coverage shows that the pinning force remains constant and the resultant pinning effects are scalable by the size ratio between the droplet and pattern, independent

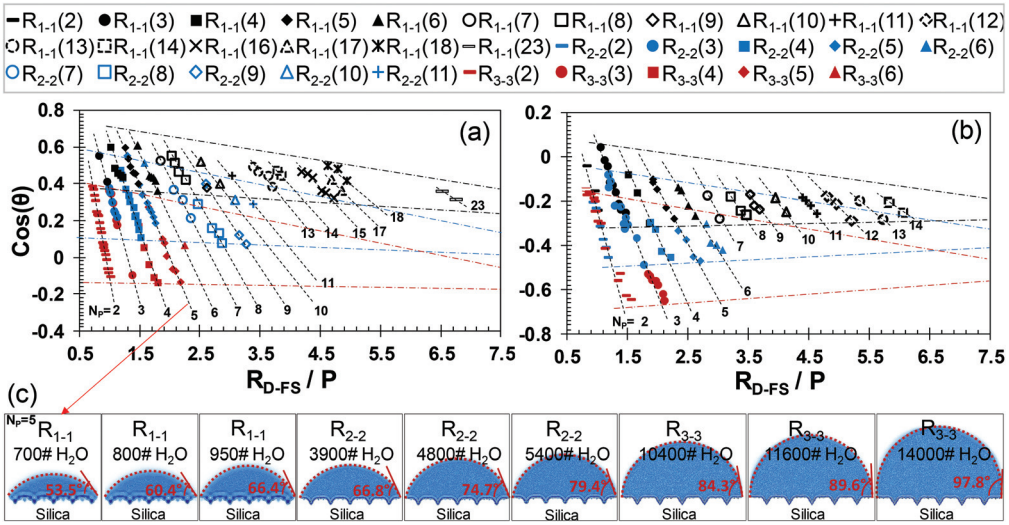

Fig. 10 Cosine of the contact angles under pinning effects as a function of the ratio between the droplet size and surface pattern size for (a) hydrophilic and (b) hydrophobic conditions. Dashed lines connect contact angles on the same number of patterns. Symbols represent number of patterns covered and colors represent the surface pattern size. (c) Density contours of complete set of the microscopic state on 5 patterns (R_{base}/P = constant). Hypothetical projections of macroscopic behavior given by dotted dashed lines estimate the equilibrium contact angles for each surface heterogeneity.

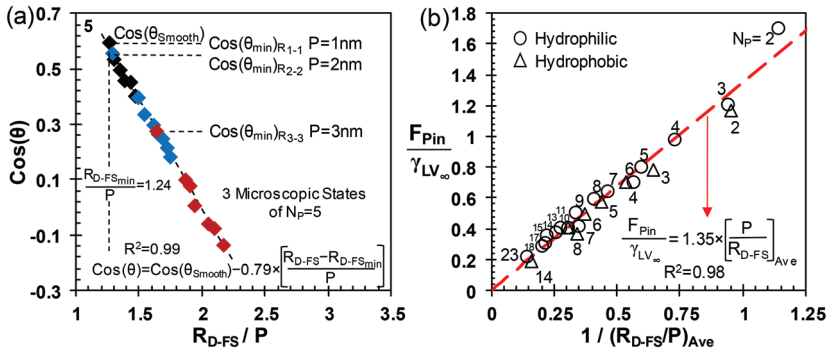

Fig. 11 (a) The continuous microscopic set of 5 pattern coverage (N_P = 5). (b) Variation of the pinning force normalized by the water surface tension as a function of the average normalized droplet size of corresponding microscopic set ($1/(R_{D\text{-}FS}/P)_{ave}$).

of the size-scale. This explains why pinning effects are observed from millimeter to nanometer scales. Here, we attempted to describe the observed variation of the contact angle for growing droplet size at a constant base area to pattern size ratio (R_{base}/P = constant). The contact angle changes linearly with the change in non-dimensional $R_{D\text{-}FS}/P$ at a constant rate which originates from pinning effects. Hence, we described the contact angle variation at a given constant R_{base}/P through the microscopic states set (3 different microscopic states of 3 different pattern sizes) as,

$$\cos\theta|_{@(R_{base}/P)=\text{constant}} = \cos\theta_{min} - \left(\frac{R_{D\text{-}FS} - R_{D\text{-}FS_{min}}}{P} \times \frac{F_{pin}}{\gamma_{LV\infty}}\right)\Bigg|_{@(R_{base}/P)=\text{constant}} \quad (9)$$

where θ_{min} is the minimum contact angle of the given microscopic set developing at $R_{D\text{-}FSmin}$, and F_{pin} is pinning force per length of the contact line (N m^{-1}). Here, $\cos\theta$ varies by $R_{D\text{-}FS}$ as a function of two unknowns as $\cos\theta_{min}$ and $F_{pin}/\gamma_{LV_\infty}$. First, the minimum contact angle value, also called the receding angle, changes from case to case. Here, we do not have enough data, but hypothesize about the possible physical development and scalable behavior of this minimum contact angle. First, we did not observe any contact angle value significantly smaller than the angle measured on the smooth surface of the corresponding wetting condition. For example, for hydrophilic cases, the lowest angle is just a few degrees different from 55°. Secondly, the lowest angle of a continuous microscopic set develops at the lowest roughness level, R_1 surface, which has molecular level heterogeneities on the order of 0.5 nm. With the increase of roughness size, this minimum contact angle increases for the following microscopic sets of larger heterogeneities. We described this occurrence in Fig. 11(a) for wetting of 5 surface patterns of different sizes under pinning effects.

Starting from the smooth surface wetting angle, the minimum angle developing through microscopic behavior on a certain number of patterns increases with the increase of roughness size. Hence, we believe that the receding angle of heterogeneous surface pinning can be correlated with the wetting angle of the smooth surface condition as a measure for the work of adhesion of the given liquid–solid couple ($\cos\theta_{min} = \cos\theta_{smooth}$ for low R_{base}/P). However, this behavior is valid for low surface pattern coverages approximately up to 8 and 4 for hydrophilic and hydrophobic conditions, respectively. With the increase of $R_{D\text{-}FS}/P$ in the macroscopic behavior, the minimum angle of microscopic sets in Fig. 10 increases. This is basically due to decreasing pinning effects and contact angles converging to the equilibrium angle of the corresponding heterogeneity, which is different from the angle of the smooth surface case. Unfortunately, it is hard to characterize this behavior, especially for hydrophobic cases.

Secondly, we attempt to characterize the behavior of pinning force of each microscopic state. We simply calculated the non-dimensional $F_{pin}/\gamma_{LV_\infty}$ value of each microscopic state set described in Fig. 10 based on eqn (9). Next, we calculated an average value of $R_{D\text{-}FS}/P$ through the corresponding microscopic set. Instead of using the number of pattern coverage (N_P) or droplet base size (R_{base}), we chose to continue to use the droplet volume since it is an easy parameter to define for experiments. These normalized pinning forces are given in Fig. 11(b) as a function of the corresponding average droplet size to pattern size ratio $(1/(R_{D\text{-}FS}/P)_{Ave})$ for both hydrophilic and hydrophobic conditions. Similar to our observations from Fig. 10, slopes of microscopic sets of hydrophilic and hydrophobic surfaces are found very similar and eventually their variation by the normalized droplet radius is found almost identical through a linear dependence to $1/(R_{D\text{-}FS}/P)_{Ave}$. This is another very interesting finding. As we were hypothesizing that the droplet volume is a better measure for pinning forces, we found a universal behavior for microscopic contact angle variation and for the corresponding pinning effect through the macroscopic variation as a function of $R_{D\text{-}FS}/P$. This universal behavior is independent of the heterogeneity size and wetting condition.

The normalized microscopic pinning force is found to decrease with the increase of the number of patterns covered. We should underline here that, what we measure is not the pinning force, instead this is its influence. Hence, Fig. 11(b) describes the macroscopic behavior of pinning for microscopic states. Another interesting aspect here is that similar pinning effects develop at lower surface pattern coverage in hydrophobic cases. For example, 8 surface patterns covered the hydrophobic case which develops a similar pinning effect to 5 surface patterns covering the hydrophilic case. This shows that the pinning effect is actually scalable with the droplet size, not the size of the droplet base.

The current literature (eqn (4)) describes the pinning effects through the macroscopic behavior as an inverse linear function of base radius ($1/R_{base}$). This perspective calculates the length of contact line on which pinning force acts and describes the macroscopic behavior with increasing droplet size. But, this perspective (eqn (4)) does not include any description for microscopic behavior for the R_{base} which is a constant value. Instead, we used a normalized droplet size which could characterize the pinning effects in both microscopic and macroscopic behavior. We applied a linear fit on the data as a function of $1/(R_{D\text{-}FS}/P)_{Ave}$. Including this approximation of pinning effect variation into eqn (9) as,

$$\cos\theta|_{@(R_{base}/P)=cnstant} = \cos\theta_{min} - 1.35 \times \left(\frac{R_{D\text{-}FS} - R_{D\text{-}FS_{min}}}{R_{D\text{-}FS_{Ave}}}\right)\Bigg|_{@(R_{base}/P)=constant} \quad (10)$$

Here, eqn (10) tells us that the contact angles under the pinning effect change as a linear function of droplet size at a certain R_{base}/P value, independent of the pattern size for any kind of high or low wetting surfaces. This is the microscopic pinning behavior including its change through macroscopic behavior. The contact angle varies between minimum and maximum values of the corresponding base radius value.

As the final step, we will focus on macroscopic behavior and try to predict the equilibrium contact angle of the corresponding heterogeneous surface without pinning effects. We observed that the contact angle is a linear function of the droplet radius with a constant pinning effect while this pinning effect changes as an inverse linear function of droplet radius. In Fig. 10, we added linear approximations to minimum and maximum angle variation of each microscopic set. These dotted dashed lines depict the linear microscopic variation of contact angles with a decreasing slope while the microscopic behavior of each surface pattern case is confined between them. Hypothetical projections of these lines intersect approximately at the equilibrium contact angle of corresponding surface heterogeneity as the slope of microscopic behaviors becomes zero as described in Fig. 11(b). Corresponding equilibrium contact angle estimations of each surface are presented in Table 2. We observed that the equilibrium contact angle increases with the increase of surface heterogeneity. For the hydrophilic condition, the contact angle increases from the smooth surface value of 55° to 73°, 87° and 100° on R_1, R_2 and R_3 patterns, respectively. For hydrophobic cases, the contact angle increases from 95° to 106°, 105° and 125° with the increase of the surface structure size. The influence of surface heterogeneity was found to be stronger under hydrophilic conditions similar to the literature.[73,74] Results also clearly show that the hydrophilic smooth surface can be

Table 2 The equilibrium contact angles of hydrophilic and hydrophobic surfaces with different heterogeneity sizes at the limit $1/R_{D\text{-}FS} \rightarrow 0$ as the pinning effects become negligible

	Smooth	R_1	R_2	R_3
Hydrophilic	55.0°	73.0°	87.0°	100.0°
Hydrophobic	95.0°	106.0°	115.0°	125.0°

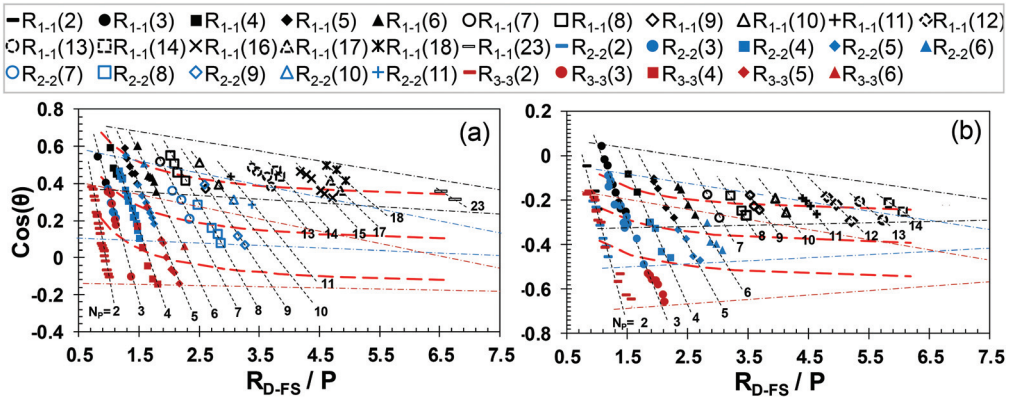

Fig. 12 Inverse linear fits to approximate the average contact angles of microscopic sets through the macroscopic behavior as the $1/R_{D\text{-}FS} \rightarrow 0$ for (a) hydrophilic and (b) hydrophobic conditions.

tuned to hydrophobic by structuring it. Another important conclusion here is about the size limit for pinning effects. With the increase of droplet size, the minimum and maximum angles of microscopic sets converge towards each other and the gradient of contact angle variation between them decreases. For the latter, we calculated the limit of linear function given in Fig. 11. We found that the slope of microscopic sets decreases to its 10% when the size ratio between the droplet radius and surface structure is approximately equal to 12. This result is also consistent with the behavior of minimum and maximum angles of microscopic sets approximated by linear lines in Fig. 10, which coincides around the $R_{D\text{-}FS}/P$ ~12 value. Hence, pinning effects become negligible when the free-standing droplet diameter is approximately equal to 24 times the size of the surface heterogeneity.

Next, we also wanted to test inverse linear dependence of pinning effects. So, we applied an approximate inverse linear function fit onto Fig. 10(a) and (b) in Fig. 12, for general characterization of pinning effects through the average contact angles of each microscopic set in macroscopic behavior. We kept the linear estimations as a projectile for the equilibrium angle at the limit $1/R_{D\text{-}FS} \rightarrow 0$ and for this figure as well.

Even though it reaches the same equilibrium contact angle at the limit for negligible pinning, Fig. 12 shows that the inverse linear relationship between pinning and the droplet size cannot properly describe the general macroscopic behavior. For the description of behavior at the limit $1/R_{D\text{-}FS} \rightarrow 0$, we also tried to curve fit of a power series. We observed that the power function of $R_{D\text{-}FS}{}^{-0.5}$ can describe the overall behavior of average microscopic contact angles through the macroscopic behavior better.

5. Conclusions

Wetting on silica surfaces is studied by MD simulations of three different surface morphologies under two different wetting conditions. Our results show that the wetting angle of nanopatterned surfaces changes depending on the droplet volume. Variation of the contact angle shows repeating increasing and decreasing oscillating behavior with the increase of volume due to the pinning forces developing on the three-phase contact line. These wetting oscillations repeat itself with decreasing the oscillation gap and eventually the contact angle converges to a certain equilibrium value as the droplet size grows. Through this study, we (i) described the size limit for pinning effects to become negligible and (ii) characterized the general contribution of pinning force. First, we presented that the contact angle varies linearly with droplet size growth at a constant droplet base size at pinned state. We refer to this behavior as "microscopic behavior". Here, we observed that pinning effects are related to the droplet size calculated directly from the droplet volume ($R_{D\text{-}FS}$), independent of the droplet shape forming at the corresponding wetting situation. A "similitude" between the wetting behaviors of different size droplets over different size heterogeneities was obtained as a function of free-standing droplet radius normalized with the pattern size of the corresponding surface ($R_{D\text{-}FS}/P$). This is one of the most important findings of the current study. When the ratio of droplet size to heterogeneity size is the same, the contact angle variation showed a universal behavior at a constant linear variation independent of the size of droplet and surface pattern. Second, we characterized the change of contact angles in each microscopic set by determining the gradient of these linear variations. Also identified as the pinning influence on Young's estimations, we further observed a universal behavior in the variation of microscopic set slopes independent of surface wetting condition. These contact angle gradients of each microscopic set decreased as an inverse linear function of average normalized droplet size of a given microscopic set ($(1/(R_{D\text{-}FS}/P)_{ave})$). To this extent, pinning effects are found as a function of $R_{D\text{-}FS}/P$ independent of the droplet size, surface heterogeneity size and wetting condition. With an increase in the droplet size, pinning influence lessens and becomes negligible, and the contact angle reaches its equilibrium value depending on heterogeneity and wetting conditions of the corresponding surface. We identified this as "macroscopic behavior". Specifically, we found that pinning

influence disappears, when the diameter of the free-standing droplet is approximately equal to 24 times the size of the surface structure.

Conflicts of interest

There are no conflicts to declare.

Acknowledgements

This work was supported by the Scientific and Technological Research Council of Turkey (TÜBİTAK) under the Grant Number 217M460. The authors would like to thank the Center for Scientific Computation at Southern Methodist University. Dr Barisik also acknowledges the support from the Turkish Academy of Sciences (TUBA) in the framework of the Young Scientist Award Programme (GEBIP).

References

1 H. G. Ozcelik and M. Barisik, Electric Charge of Nanopatterned Silica Surfaces, *Phys. Chem. Chem. Phys.*, 2019, **21**(14), 7576–7587.
2 S.-H. Jeon, W.-I. Choi, G.-D. Song, Y.-H. Son and D. H. Hur, Influence of Surface Roughness and Agitation on the Morphology of Magnetite Films Electrodeposited on Carbon Steel Substrates, *mdpi.com*, 2016, **6**(4), 62, DOI: 10.3390/coatings6040062.
3 C. Yiannakou, C. Simitzi, A. Manousaki, C. Fotakis, A. Ranella and E. Stratakis, Cell Patterning via Laser Micro/Nano Structured Silicon Surfaces, *Biofabrication*, 2017, **9**(2), 025024.
4 S. Zhou, B. Zheng, Y. Shimotsuma, Y. Lu, Q. Guo, M. Nishi, M. Shimizu, K. Miura, K. Hirao and J. Qiu, Heterogeneous-Surface-Mediated Crystallization Control, *NPG Asia Mater.*, 2016, **8**(3), e245.
5 R. N. Wenzel, Resistance of Solid Surfaces to Wetting by Water, *Ind. Eng. Chem.*, 1936, **28**(8), 988–994.
6 A. B. D. Cassie and S. Baxter, Wettability of Porous Surfaces, *Trans. Faraday Soc.*, 1944, **40**, 546–551.
7 J. E. Andrews, Y. Wang, S. Sinha, P. W. Chung and S. Das, Roughness-Induced Chemical Heterogeneity Leads to Large Hydrophobicity in Wetting-Translucent Nanostructures, *J. Phys. Chem. C*, 2017, **121**(18), 10010–10017, DOI: 10.1021/acs.jpcc.7b02222.
8 C. Huang, F. Xu and Y. Sun, Effects of Morphology, Tension and Vibration on Wettability of Graphene: A Molecular Dynamics Study, *Comput. Mater. Sci.*, 2017, **139**, 216–224, DOI: 10.1016/j.commatsci.2017.07.017.
9 J. F. Oliver, C. Huh and S. G. Mason, Resistance to Spreading of Liquids by Sharp Edges, *J. Colloid Interface Sci.*, 1977, **59**(3), 568–581, DOI: 10.1016/0021-9797(77)90052-2.
10 L. Gao and T. J. McCarthy, Contact Angle Hysteresis Explained, *Langmuir*, 2006, **22**(14), 6234–6237.
11 D. C. Pease, The Significance of the Contact Angle in Relation to the Solid Surface, *J. Phys. Chem.*, 1945, **49**(2), 107–110.
12 J. Liu, Y. Mei and R. Xia, A New Wetting Mechanism Based upon Triple Contact Line Pinning, *Langmuir*, 2011, **27**(1), 196–200.
13 Z. Yoshimitsu, A. Nakajima, T. Watanabe and K. Hashimoto, Effects of Surface Structure on the Hydrophobicity and Sliding Behavior of Water Droplets, *Langmuir*, 2002, **18**(15), 5818–5822.
14 F. C. Wang and H. A. Wu, Pinning and Depinning Mechanism of the Contact Line during Evaporation of Nano-Droplets Sessile on Textured Surfaces, *Soft Matter*, 2013, **9**(24), 5703–5709, DOI: 10.1039/c3sm50530h.
15 X. Chen, R. Ma, J. Li, C. Hao, W. Guo, B. L. Luk, S. C. Li, S. Yao and Z. Wang, Evaporation of Droplets on Superhydrophobic Surfaces: Surface Roughness and Small Droplet Size Effects, *Phys. Rev. Lett.*, 2012, **109**(11), 116101.
16 J. Zhang, F. Müller-Plathe and F. Leroy, Pinning of the Contact Line during Evaporation on Heterogeneous Surfaces: Slowdown or Temporary Immobilization? Insights from a Nanoscale Study, *Langmuir*, 2015, **31**(27), 7544–7552.
17 D. Kim, N. M. Pugno and S. Ryu, Wetting Theory for Small Droplets on Textured Solid Surfaces, *Sci. Rep.*, 2016, **6**, 37813.
18 F. C. Wang and H. A. Wu, Molecular Origin of Contact Line Stick-Slip Motion during Droplet Evaporation, *Sci. Rep.*, 2015, **5**, 17521.
19 E. Dietrich, E. S. Kooij, X. Zhang, H. J. W. Zandvliet and D. Lohse, Stick-Jump Mode in Surface Droplet Dissolution, *Langmuir*, 2015, **31**(16), 4696–4703.
20 Y. Liu and X. Zhang, Nanobubble Stability Induced by Contact Line Pinning, *J. Chem. Phys.*, 2013, **138**(1), 014706.
21 H. Zhang, S. Chen, Z. Guo, Y. Liu, F. Bresme and X. Zhang, Contact Line Pinning Effects Influence Determination of the Line Tension of Droplets Adsorbed on Substrates, *J. Phys. Chem. C*, 2018, **122**(30), 17184–17189.
22 P. S. H. Forsberg, C. Priest, M. Brinkmann, R. Sedev and J. Ralston, Contact Line Pinning on Microstructured Surfaces for Liquids in the Wenzel State, *Langmuir*, 2010, **26**(2), 860–865.
23 T. Pompe and S. Herminghaus, Three-Phase Contact Line Energetics from Nanoscale Liquid Surface Topographies, *Phys. Rev. Lett.*, 2000, **85**(9), 1930–1933.
24 N. Bruot and F. Caupin, Curvature Dependence of the Liquid-Vapor Surface Tension beyond the Tolman Approximation, *Phys. Rev. Lett.*, 2016, **116**(5), 056102.
25 L. Schimmele, M. Naplórkowski and S. Dietrich, Conceptual Aspects of Line Tensions, *J. Chem. Phys.*, 2007, **127**(16), 164715.
26 A. Malijevsk and G. Jackson, A Perspective on the Interfacial Properties of Nanoscopic Liquid Drops, *J. Phys.: Condens. Matter*, 2012, **24**(46), 464121.

27 H. G. Ozcelik, A. C. Ozdemir, B. Kim and M. Barisik, Wetting of Single Crystalline and Amorphous Silicon Surfaces: Effective Range of Intermolecular Forces for Wetting, *Mol. Simul.*, 2020, **46**(3), 224–234.
28 M. Schrader, P. Virnau and K. Binder, Simulation of Vapor-Liquid Coexistence in Finite Volumes: A Method to Compute the Surface Free Energy of Droplets, *Phys. Rev. E: Stat., Nonlinear, Soft Matter Phys.*, 2009, **79**(6), 061104.
29 Ø. Wilhelmsen, D. Bedeaux and D. Reguera, Tolman Length and Rigidity Constants of the Lennard-Jones Fluid, *J. Chem. Phys.*, 2015, **142**(6), 064706.
30 J. Y. Wang, S. Betelu and B. M. Law, Line Tension Approaching a First-Order Wetting Transition: Experimental Results from Contact Angle Measurements, *Phys. Rev. E: Stat., Nonlinear, Soft Matter Phys.*, 2001, **63**(3), 031601.
31 R. C. Tolman, The Effect of Droplet Size on Surface Tension, *J. Chem. Phys.*, 1949, **17**(3), 333–337.
32 M. Kanduč, Going beyond the Standard Line Tension: Size-Dependent Contact Angles of Water Nanodroplets, *J. Chem. Phys.*, 2017, **147**(17), 174701.
33 J. Zhang, P. Wang, M. K. Borg, J. M. Reese and D. Wen, A Critical Assessment of the Line Tension Determined by the Modified Young's Equation, *Phys. Fluids*, 2018, **30**(8), 082003.
34 G. Scocchi, D. Sergi, C. D'Angelo and A. Ortona, Wetting and contact-line effects for spherical and cylindrical droplets on graphene layers: A comparative molecular-dynamics investigation, *Phys. Rev. E: Stat., Nonlinear, Soft Matter Phys.*, 2011, **84**(6), 061602.
35 J. H. Weijs, Antonin Marchand, Bruno Andreotti, Detlef Lohse, and Jacco H. Snoeijer., Origin of line tension for a Lennard-Jones nanodroplet, *Phys. Fluids*, 2011, **23**(2), 022001.
36 M. E. M. Azouzi, C. Ramboz, J. F. Lenain and F. Caupin, A Coherent Picture of Water at Extreme Negative Pressure, *Nat. Phys.*, 2013, **9**(1), 38–41.
37 M. N. Joswiak, N. Duff, M. F. Doherty and B. Peters, Size-Dependent Surface Free Energy and Tolman-Corrected Droplet Nucleation of TIP4P/2005 Water, *J. Phys. Chem. Lett.*, 2013, **4**(24), 4267–4272.
38 B. B. Wang, Y. P. Zhao and T. Yu, Fabrication of Novel Superhydrophobic Surfaces and Droplet Bouncing Behavior - Part 2: Water Droplet Impact Experiment on Superhydrophobic Surfaces Constructed Using ZnO Nanoparticles, *J. Adhes. Sci. Technol.*, 2011, **25**(1–3), 93–108.
39 F. C. Wang and Y. P. Zhao, Contact Angle Hysteresis at the Nanoscale: A Molecular Dynamics Simulation, *Colloid Polym. Sci.*, 2013, **291**(2), 307–315.
40 M. Vallet-Regí, M. Colilla, I. Izquierdo-Barba and M. Manzano, Mesoporous Silica Nanoparticles for Drug Delivery: Current Insights, *Molecules*, 2018, **23**(1), 47.
41 Y. P. Ying, S. K. Kamarudin and M. S. Masdar, Silica-Related Membranes in Fuel Cell Applications: An Overview, *Int. J. Hydrogen Energy*, 2018, **43**(33), 16068–16084.
42 S. Plimpton, Fast Parallel Algorithms for Short-Range Molecular Dynamics, *J. Comput. Phys.*, 1995, **117**(1), 1–19, DOI: 10.1006/jcph.1995.1039.
43 S. Iarlori, D. Ceresoli, M. Bernasconi, D. Donadio and M. Parrinello, Dehydroxylation and Silanization of the Surfaces of β-Cristobalite Silica: An Ab Initio Simulation, *J. Phys. Chem. B*, 2001, **105**(33), 8007–8013.
44 P. N. Plessow, R. S. Sánchez-Carrera, L. Li, M. Rieger, S. Sauer, A. Schaefer and F. Abild-Pedersen, Modeling the Interface of Platinum and α-Quartz(001): Implications for Sintering, *J. Phys. Chem. C*, 2016, **120**(19), 10340–10350.
45 J. Tersoff, New Empirical Approach for the Structure and Energy of Covalent Systems, *Phys. Rev. B: Condens. Matter Mater. Phys.*, 1988, **37**(12), 6991–7000, DOI: 10.1103/PhysRevB.37.6991.
46 S. Munetoh, T. Motooka, K. Moriguchi and A. Shintani, Interatomic Potential for Si-O Systems Using Tersoff Parameterization, *Comput. Mater. Sci.*, 2007, **39**(2), 334–339, DOI: 10.1016/j.commatsci.2006.06.010.
47 S. Miyamoto and P. A. Kollman, Settle: An Analytical Version of the SHAKE and RATTLE Algorithm for Rigid Water Models, *J. Comput. Chem.*, 1992, **13**(8), 952–962, DOI: 10.1002/jcc.540130805.
48 A. K. Al-Matar and D. A. Rockstraw, A Generating Equation for Mixing Rules and Two New Mixing Rules for Interatomic Potential Energy Parameters, *J. Comput. Chem.*, 2004, **25**(5), 660–668.
49 M. Barisik and A. Beskok, Wetting Characterisation of Silicon (1,0,0) Surface, *Mol. Simul.*, 2013, **39**(9), 700–709, DOI: 10.1080/08927022.2012.758854.
50 W. Kohn and L. J. Sham, Self-Consistent Equations Including Exchange and Correlation Effects, *Phys. Rev.*, 1965, **140**, A1133, DOI: 10.1103/PhysRev.140.A1133.
51 B. Ramos-Alvarado, S. Kumar and G. P. Peterson, Wettability of Graphitic-Carbon and Silicon Surfaces: MD Modeling and Theoretical Analysis, *J. Chem. Phys.*, 2015, **143**(4), 044703.
52 T. Q. Vo, M. Barisik and B. Kim, Near-surface viscosity effects on capillary rise of water in nanotubes, *Phys. Rev. E: Stat., Nonlinear, Soft Matter Phys.*, 2015, **92**(5), 053009.
53 M. Fyta and R. R. Netz, Ionic Force Field Optimization Based on Single-Ion and Ion-Pair Solvation Properties: Going beyond Standard Mixing Rules, *J. Chem. Phys.*, 2012, **136**(12), 124103.
54 T. Werder, J. H. Walther, R. L. Jaffe, T. Halicioglu and P. Koumoutsakos, On the Water-Carbon Interaction for Use in Molecular Dynamics Simulations of Graphite and Carbon Nanotubes, *J. Phys. Chem. B*, 2003, **107**(6), 1345–1352, DOI: 10.1021/jp0268112.
55 E. R. Cruz-Chu, A. Aksimentiev and K. Schulten, Water-Silica Force Field for Simulating Nanodevices, *J. Phys. Chem. B*, 2006, **110**(43), 21497–21508, DOI: 10.1021/jp063896o.
56 J. Klimeš and A. Michaelides, Perspective: Advances and Challenges in Treating van Der Waals Dispersion Forces in

Density Functional Theory, *J. Chem. Phys.*, 2012, **137**(12), 120901.

57 A. D. Becke, Real-Space Post-Hartree-Fock Correlation Models, *J. Chem. Phys.*, 2005, **122**(6), 064101.

58 A. Tkatchenko and M. Scheffler, Accurate Molecular van Der Waals Interactions from Ground-State Electron Density and Free-Atom Reference Data, *Phys. Rev. Lett.*, 2009, **102**(7), 073005.

59 A. D. Becke and E. R. Johnson, A Density-Functional Model of the Dispersion Interaction, *J. Chem. Phys.*, 2005, **123**(15), 154101.

60 E. R. Johnson and A. D. Becke, A Post-Hartree-Fock Model of Intermolecular Interactions: Inclusion of Higher-Order Corrections, *J. Chem. Phys.*, 2006, **124**(17), 174104.

61 H. G. Ozcelik, Y. Sozen, H. Sahin and M. Barisik, Parametrizing Nonbonded Interactions between Silica and Water from First Principles, *Appl. Surf. Sci.*, 2020, **504**, 144359.

62 S. Iglauer, A. Salamah, M. Sarmadivaleh, K. Liu and C. Phan, Contamination of Silica Surfaces: Impact on Water-CO2-Quartz and Glass Contact Angle Measurements, *Int. J. Greenhouse Gas Control*, 2014, **22**, 325–328, DOI: 10.1016/j.ijggc.2014.01.006.

63 M. Annamalai, K. Gopinadhan, S. A. Han, S. Saha, H. J. Park, E. B. Cho, B. Kumar, A. Patra, S. W. Kim and T. Venkatesan, Surface Energy and Wettability of van Der Waals Structures, *Nanoscale*, 2016, **8**(10), 5764–5770, DOI: 10.1039/c5nr06705g.

64 R. Raj, S. C. Maroo and E. N. Wang, Wettability of Graphene, *Nano Lett.*, 2013, **13**(4), 1509–1515, DOI: 10.1021/nl304647t.

65 C. J. Shih, Q. H. Wang, S. Lin, K. C. Park, Z. Jin, M. S. Strano and D. Blankschtein, Breakdown in the Wetting Transparency of Graphene, *Phys. Rev. Lett.*, 2012, **109**(17), 176101.

66 M. Barisik and A. Beskok, Equilibrium Molecular Dynamics Studies on Nanoscale-Confined Fluids, *Microfluid. Nanofluid.*, 2011, **11**(3), 269–282.

67 J. W. Gibbs, ART. LII. – On the Equilibrium of Heterogeneous Substances, *Am. J. Sci. Arts*, 1878, **16**(96), 441.

68 Y. Liu, J. Wang and X. Zhang, Accurate determination of the vapor-liquid-solid contact line tension and the viability of Young equation, *Sci. Rep.*, 2013, **3**, 2008.

69 S. Nishida, D. Surblys, Y. Yamaguchi, K. Kuroda, M. Kagawa, T. Nakajima and H. Fujimura, Molecular dynamics analysis of multiphase interfaces based on in situ extraction of the pressure distribution of a liquid droplet on a solid surface, *J. Chem. Phys.*, 2014, **140**(7), 074707.

70 Y. Yamaguchi, H. Kusudo, D. Surblys, T. Omori and G. Kikugawa, Interpretation of Young's equation for a liquid droplet on a flat and smooth solid surface: Mechanical and thermodynamic routes with a simple Lennard-Jones liquid, *J. Chem. Phys.*, 2019, **150**(4), 044701.

71 J. Zhang, H. Huang and X.-Y. Lu, Pinning–Depinning Mechanism of the Contact Line during Evaporation of Nanodroplets on Heated Heterogeneous Surfaces: A Molecular Dynamics Simulation, *Langmuir*, 2019, **35**(19), 6356–6366.

72 Z. Wang, K. Lin and Y.-P. Zhao, The effect of sharp solid edges on the droplet wettability, *J. Colloid Interface Sci.*, 2019, **552**, 563–571.

73 C. T. Nguyen, M. Barisik and B. Kim, Wetting of Chemically Heterogeneous Striped Surfaces: Molecular Dynamics Simulations, *AIP Adv.*, 2018, **8**(6), 065003.

74 D. M. Spori, T. Drobek, S. Zürcher, M. Ochsner, C. Sprecher, A. Mühlebach and N. D. Spencer, Beyond the Lotus Effect: Roughness Influences on Wetting over a Wide Surface-Energy Range, *Langmuir*, 2008, **24**(10), 5411–5417.